Supporting Information for

Core-mantle boundary dynamic topography: influence of post-perovskite viscosity

Frédéric Deschamps[1], Yang Li[2]

[1] Institute of Earth Sciences, Academia Sinica, 128 Academia Road, 11529 Taipei, Taiwan, [2] State Key Laboratory of Lithospheric Evolution, Institute of Geology and Geophysics, Chinese Academy of Sciences, Beijing, China.

Contents of this file

Additional Supporting Information (Files uploaded separately)

Introduction

Supplementary material contains Text S1 to S3, with technical details on the numerical modelling and simulations setups, details on the definitions of plumes and downwellings regions and on the calculation of shear-wave velocity anomalies from the distributions of temperature and compositions obtained by numerical simulations, Supplementary Table S1 listing parameters and scalings of the simulations, and Supplementary Figures S1 to S8.

Text S1 - Details of numerical simulations.

The numerical setup used to model thermal and thermo-chemical convection in Earth's mantle is essentially the same as that used in the numerical simulations of Deschamps et al. (2018). Conservation equations of mass, energy, momentum and composition are solved for a compressible, infinite Prandtl number fluid using the software StagYY (Tackley, 2008). Details of the numerical techniques used to solve this system of equations may be found in

Tackley (2008). All calculations are performed in non-dimensional values. The main properties of the models calculated in this study are detailed below, and values of input and scaling parameters are listed in Table S1.

Geometry and general physical properties. Conservation equations are solved in spherical shells sampled by 128 horizontal layers. Each layer is modelled with the combination of a Yin and a Yang grid of 384×128 nodes, leading to a lateral resolution of 512×256 points. The ratio between the radius of the core and the total radius is set to its Earth value, *i.e.* $f = 0.55$. The bottom and surface boundaries are free slip. The system is heated both from the bottom and from within, with a total mantle heating rate equivalent to a surface heat flux of 10 mW/m² and a ratio of internal to basal heating close to 0.3. Note that, because primordial material may be enriched in radiogenic elements (*e.g.*, Richter et al., 1985; Kellog et al., 1999), and following Deschamps et al. (2008), we increased the rate of internal heating in primordial material by a factor 10 compared to the regular mantle. Compressibility generates additional sinks and sources of heat that are controlled by the dissipation number, *Di*, which varies with depth following

$$Di(z) = \frac{\alpha(z)gD}{C_P},$$ (A1)

where α is the thermal expansion, g the acceleration of gravity, D the shell's thickness, and C_P the heat capacity (here assumed constant throughout the system). The surface value of this number is set to $Di_S = 1.2$, and the depth variations of thermal expansion imply that its volume average is equal to 0.43. Because the fluid properties (density, viscosity, thermal diffusivity, and thermal expansion) are allowed to vary throughout the system (next paragraph), the definition of the Rayleigh number is non-unique. In our simulations, we prescribed a reference Rayleigh number Ra_0, defined at surface values of the thermodynamic parameters and reference viscosity η_0. Here, Ra_0 is set to 3.0×10⁸, leading to an effective Rayleigh number (*i.e.*, the Rayleigh number at the volume average viscosity) in the range 10⁶ and 2.0×10⁶, for, depending on the model.

Reference thermodynamical model. The conservation equations involve the definition of a thermodynamic reference state, which here consists of a set of vertical profiles for density, temperature, and thermal expansion calculated using thermodynamic relationships for the Earth's mantle (Tackley, 1998). Reference temperature is scaled with respect to the super-adiabatic temperature difference across the system, ΔT_S, which is here fixed to 2500 K, and reference density and thermal expansion are scaled with respect to their surface values. In particular, the reference density increases by about a factor 1.5 from top to bottom, including a discontinuity at the limit between upper and lower mantle with non-dimensional amplitude of about 0.12 (equivalent to a dimensional value of 400 kg/m³). The reference temperature corresponds to a non-dimensional adiabat of 0.64 (equivalent to 1600 K), and increases with depth up to a non-dimensional value of 1.55. Thermal expansion decreases by a factor 5 from surface to bottom, and the Grüneisen parameter, γ_{ref}, varies in such a way that its product with reference density is constant with depth. Thermodynamic properties used to build the reference state are listed in Table S1 together with other scalings and properties.

Thermochemical field. Thermo-chemical models distinguish two types of material, regular mantle and chemically distinct, or primordial, material. The latter accounts for chemical heterogeneities that may be present at the bottom of the mantle as a result of early differentiation. The compositional field is modelled with a collection of 200 million of tracers, leading to an average number of tracers per cell of about 15, which is enough to properly

model entrainment (Tackley and King, 2003). Tracers are of two types, modelling the regular mantle and primordial material, respectively, and are advected following a 4th order Runge-Kutta method. At each time step, the compositional field is inferred from the concentration C of particles of primordial material in each cell, and varies between 0 for a cell filled with regular material only, and 1 for a cell filled with primordial material only. The exact nature of the compositional field is not prescribed *a-priori* (except for its density excess) and can be fixed by the user during post-processing. Here, prescribing the nature of the compositional field only matters for the calculation of seismic velocity anomalies, and it is assumed that the regular mantle is pyrolitic, and that the primordial material is enriched in iron oxide and bridgmanite. The primordial material is initially distributed in a basal layer, the thickness of which is controlled by the volume fraction of dense material, X_{prim}, following

$$h_{DL} = \frac{\left[X_{prim}(1-f^3)+f^3\right]^{1/3}-f}{(1-f)},$$ (A2)

where f is, again, the ratio of inner to outer shell radii. Here, X_{prim} is set to 3.5% in all models, which, for $f = 0.55$ leads to an initial thickness of the dense material layer $h_{DL} = 0.068$. The primordial material is further assumed to be denser than the regular (pyrolitic) mantle, and the density contrast between the two types of materials is controlled by the buoyancy ratio, here defined with respect to a reference density that increases with depth following a thermodynamical model of Earth's mantle,

$$B_z = \frac{\Delta\rho_c(z)}{\alpha_s\rho(z)\Delta T_S},$$ (A3)

where $\Delta\rho_c(z)$ is the density contrast between dense and regular material, α_s the surface thermal expansion, $\rho(z)$ the reference density at depth z, and ΔT_S the super-adiabatic temperature jump. In our simulations, we fixed the buoyancy ratio either to $B_z = 0.23$ (models TC1 to TC4) or to $B_z = 0.15$ (models TC5 and TC6). At the bottom of the system, and taking $\alpha_s = 5.0\times10^{-5}$ K^{-1}, $\rho_{bot} = 4950$ kg m^{-3}, and $\Delta T_S = 2500$ K, this leads to a density contrast between dense and regular material around 142 and 93 kg m^{-3}, respectively. Following Eq. (A3) the reference density increases with depth while B_z remains constant, implying that the chemical density contrast increases with depth proportionally to the reference density. With this definition, the buoyancy ratio required to obtain a chemical stratification of the system is smaller than when the surface density is taken as reference density. For equivalent chemical density contrast at the bottom of the system, however, results of the simulations do not differ substantially.

As convection starts and develop in the system, primordial material is entrained by the flow and mixes with regular material. The efficiency of mixing depends on the input parameters, mainly the buoyancy ratio, and can be measured with the average altitude at which primordial is located, $<h_C>$, defined as

$$<h_C> = \frac{1}{V}\int C(r,\theta,\varphi)hdV,$$ (A4)

where V is the volume of the shell. The value of $<h_C>$ varies from h_{DL} (Eq. A1) in the case of strong chemical stratification, to

$$h_{mix} = \frac{\left(\frac{1+f^3}{2}\right)^{1/3}-f}{(1-f)},$$ (A5)

for a full mixing between primordial and regular materials. For $f = 0.55$, $h_{mix} = 0.634$. Values of $<h_C>$ for the simulations performed in this study are listed in Table 1 (main article).

Viscosity. Viscosity is allowed to vary with depth, temperature, and composition. Additional viscosity ratios at the 660-km discontinuity between upper and lower mantles, $\Delta\eta_{660}$, and at the transition to the post-perovskite phase, $\Delta\eta_{pPv}$, are also included. The viscosity ratio at 660 km is fixed to $\Delta\eta_{660} = 30$, and $\Delta\eta_{pPv}$ is chosen between 10^{-3} and 1 depending on the simulation. This allows investigating the effect of pPv viscosity on the flow and on the dynamic topography at the core-mantle boundary (CMB), in particular for low viscosity cases (Amman et al., 2010). Finally, to avoid the formation of stagnant lid at the top of the system, a yield stress is imposed. The viscosity is then fully described by

$$\eta = \frac{1}{\frac{1}{\eta_b}+\frac{1}{\eta_Y}}, \tag{A6}$$

where $\quad \eta_Y = \frac{\sigma_0+\dot{\sigma}_z P}{2\dot{e}} \tag{A7}$

is the yield viscosity, and

$$\eta_b(z,T,C) = \eta_0 \left[1 + 29H(z - 660)\right]\exp\left[V_a\frac{z}{D} + E_a\frac{\Delta T_S}{(T+T_{\text{off}})} + K_a C\right]\Delta\eta_{pPv}. \tag{A8}$$

The yield viscosity (Eq. A6) is defined from the yield stress, $\sigma_Y = \sigma_0 + \dot{\sigma}_z P$, and the second invariant of the stress tensor, $\dot{e}$. The yield stress is set to σ_0 at the surface and increases with pressure following a gradient $\dot{\sigma}_z$. In Eq. (A8) η_0 is a reference viscosity, H the Heaviside step function, z the depth, D the mantle thickness, ΔT_S the super-adiabatic temperature difference across the system, and T_{off} the temperature offset, which is added to the temperature to reduce the viscosity jump across the top thermal boundary layer. The reference viscosity η_0 is defined for the surface value of the reference adiabat (*i.e.*, $T_{as} = 0.64\Delta T_S$), and at regular composition ($C = 0$). The viscosity variations with temperature are controlled by E_a, modelling the activation energy. The thermally-induced increase of viscosity, is quantified with a potential thermal viscosity ratio as $\Delta\eta_T = \exp(E_a)$. However, due to the adiabatic increase of temperature and to the temperature offset, which is fixed to $T_{\text{off}} = 0.88\Delta T_S$, the effective top-to-bottom thermal viscosity ratio is smaller than $\Delta\eta_T$ by about two orders of magnitude. In all the models presented in this study, E_a is set to 20.723, corresponding to $\Delta\eta_T = 10^9$. The viscosity variations with depth are controlled by the parameter V_a, modelling the activation volume, which we fix to 2.303 in all simulations. This leads to an increase of viscosity from top to bottom by a factor 300. Note that this increase includes the viscosity jump at 660 km, but excludes the decrease due to adiabatic increase of temperature and the thermally-induced increase in thermal boundary layers. The viscosity variations with composition are controlled by the parameter K_a, and the viscosity ratio between primordial and regular material (or chemical viscosity ratio) is given by $\Delta\eta_C = \exp(K_a)$. In this study, primordial material is assumed to be more viscous than regular material with $\Delta\eta_C = 30$, accounting for the fact that if dense material is enriched in bridgmanite (Trampert et al., 2004; Mosca et al., 2012), it may be more viscous than surrounding mantle (Yamazaki and Karato, 2001). Finally, viscosities of mantle materials may depend on the size of the grains composing these rocks, potentially affecting the dynamics and evolution of the mantle. A discussion on the possible effects of the viscosity variations with grain size on our simulations can be found in Deschamps et al. (2018).

Phase changes. The transformation of ringwoodite into bridgmanite and ferro-periclase at 660 km is modelled with a discontinuous phase transition controlled by defining a point on

the phase boundary and a Clapeyron slope, Γ_{660}. Here, the anchor point is set at $z = 660$ km and $T = 1900$ K, and the Clapeyron slope is set to $\Gamma_{660} = -2.5$ MPa/K. The accompanying density contrast is fixed to $\Delta\rho_{660} = 400$ kg/m^3 and is scaled with the surface density. Combined with the 660-km viscosity increase (from upper to lower mantle), the 660-km phase change has a strong influence on the geometry of the plumes. This transition acts as a negatively buoyant barrier, which results in a spreading of the plume conduit beneath this boundary, and a thinning above it. The phase transition to post-perovskite, which is expected to happen in cold regions in the deep mantle, is modelled by choosing a reference point on the pPv phase boundary, here at temperature $T_{pPv} = 2700$ K and depth z_{pPv} 2700 km. Lateral deviations in the transition depth are then determined by using the phase function approach of Christensen and Yuen (1985). Following this definition, the pPv phase function γ_{pPv} at depth z and temperature T varies between 0 for pure bridgmanite to 1 for pure post-perovskite, and is given by

$$\gamma_{\mathrm{pPv}} = 0.5 + 0.5\tanh\left[\frac{(z - z_{pPv}) + \Gamma_{pPv}(T - T_{pPv})}{w}\right],$$ (A9)

where (T_{pPv}, z_{pPv}) is the reference point on the phase boundary, Γ_{pPv} is the Clapeyron slope, and w is the width of the phase transition. The Clapeyron slope and the density contrast are set to $\Gamma_{pPv} = 13$ MPa/K (Tateno et al., 2009) and $\Delta\rho_{pPv} = 62$ kg/m^3 (corresponding to a relative contrast of ~ 1.0%, Murakami et al., 2004), respectively. Determining the stability field of pPv further requires fixing the temperature at the core-mantle boundary (CMB), T_{CMB}. Here, we fixed this parameter to 3750 K, which is slightly larger than the median value of its current estimated range (Tackley, 2012). It is further important to note that, according to the numerical simulation of Li et al. (2015), the combination $\Gamma_{pPv} = 13$ MPa/K and $T_{CMB} = 3750$ K provides a better description of lower mantle structure (as observed by seismic tomography) than other sets of these parameters.

Dynamic topography. The dynamic topography at the CMB, h_{CMB}, is calculated from the normal stress, σ_{zz}, induced by the flow on this boundary, and takes into account self-gravitational effects following Zhang et al. (1993). At each point of the CMB, dynamic topography is given by

$$h_{\mathrm{CMB}} = \frac{\sigma_{zz} + \Phi_{\mathrm{CMB}}\Delta\rho_{\mathrm{CMB}}}{\Delta\rho_{\mathrm{CMB}}g},$$ (A10)

where $\Delta\rho_{CMB}$ is the density difference between the mantle and the outer core, Φ_{CMB} the perturbation of gravitational potential at CMB, and g the acceleration of gravity. The normal stress is given by

$$\sigma_{zz} = 2\eta\left(\frac{\partial v_r}{\partial r} - \frac{1}{3}\nabla \cdot \boldsymbol{v}\right),$$ (A11)

where $\boldsymbol{v}$ is velocity and v_r its vertical component. Note that the divergence of velocity in the right hand side of Eq. (A11) is due to compressibility. Gravitational potential perturbations are obtained by solving Poisson's equation for density anomalies (with respect to the reference state) that includes thermal and chemical effects, and variations in CMB topography.

Initial conditions. In all experiments, the initial condition for temperature consists of an adiabatic profile with thin super-adiabatic boundary layers at the top and bottom of the shell, to which small random perturbations are added. With this setup, each experiment starts with a transient phase, during which the bottom layer heats up. The duration of this

phase depends on the details of the system setup, and varies from non-dimensional times of about 0.2×10^{-2} (0.85 Gyr in dimensional time) for purely thermal models, to 0.5×10^{-2} (2.1 Gyr) for thermo-chemical simulations. Note that this duration is not affected by the viscosity of post-perovskite. After this phase, the evolution of the layer of dense material depends on the input parameters, mainly the buoyancy ratio and the thermal viscosity contrast. It is important to keep in mind that the experiments discussed here are not designed to model the detailed evolution of the Earth's mantle, for which accurate initial conditions are not yet known. Instead, they aim to identify the typical thermo-chemical structure obtained for a given set of parameters, and how this structure evolve in time in time. Therefore, time indication in our experiments should not be compared with the age of the Earth, or be used to interpret early evolution.

Text S2 - Identification of plumes and downwelings.

To calculate the average topography in specific regions, more particularly downwellings, hot plumes, or thermo-chemical piles, one needs to estimate in which regions of the CMB these structures are present. Here, plumes regions at a given depth z are defined as the regions where the temperature exceeds the horizontally averaged temperature at this depth, $\bar{T}(z)$, by a fraction c_{plume} of the maximum excess temperature anomaly $i.e.$, regions where the temperature is equal to or larger than

$$T_{plume}(z) = \bar{T}(z) + c_{plume}[T_{max}(z) - \bar{T}(z)], \tag{A12}$$

where T_{max} is the maximum temperature at depth z. Equivalently, downwellings regions are defined as regions where the temperature is equal to or lower than

$$T_{slab}(z) = \bar{T}(z) - c_{slab}[\bar{T}(z) - T_{min}(z)], \tag{A13}$$

where T_{min} is the minimum temperature at depth z. Finally, thermo-chemical piles are defined as regions where the fraction of dense material C is larger than 0.5. Note that, because the transitions between dense piles and regular mantle are always very sharp, any values of C larger than 0.3 gives a good description of the size and extension of these piles above the CMB. By contrast, chosing values of c_{plume} and c_{slab} is rather subjective, and different values leads to differences in the estimated extents of plume and downwelling regions, which induce, in turn, variations in the estimated average topography within these regions. For instance, reducing c_{slab} increases the area of downwelling regions by including regions with smoother topography, thus decreasing the average topography. Importantly, while the extent of plume and slab areas influence the average CMB topography in these regions, it does not affect the expected trends, $i.e.$, plume areas induce elevations in the CMB and slabs regions cause depressions. Here, both c_{plume} and c_{slab} are fixed to 0.5, $i.e.$, boundaries of plume and downwelling regions are defined by surface where temperature anomalies with respect to horizontal average reach half the maximum positive anomaly or the maximum negative anomaly, respectively.

Text S3 - From output thermo-chemical distributions to seismic velocity structures.

Calculating shear-wave velocity anomalies (as in Figures 8 and 9) from the distributions of temperature and composition obtained by numerical simulations requires to rescale the non-dimensional temperature field issued from simulations, and to convert the rescaled

temperature and composition field to seismic velocity using appropriate seismic sensitivities. These operations that are detailed below.

Adiabatic correction and rescaling to Earth's mantle. In numerical simulations performed in this study, all calculations are done in non-dimensional units. Adiabatic effects on temperature are taken into account when solving the energy and momentum conservation equations, but for practical reasons, the output temperature fields, as those plotted in Figures 2a and 3a and Supplementary Figures S1a and S2a, do not include these effects. For calculation of shear-wave velocity anomalies or other seismic parameters, output temperature must be rescaled and corrected with the adiabatic increase of temperature with pressure. The 'real' temperature at a given location, $T_r(x,y,z)$, is then obtained from the non-dimensional, uncompressed temperature, $\tilde{T}(x, y, z)$, following

$$T_r(x, y, z) = \left[\tilde{T}(x, y, z) + \tilde{T}_{top}\right]a(z)\Delta T_S \qquad (A14)$$

where ΔT_S = 2500 K the superadiabatic temperature jump, $\tilde{T}_{top}$ is the surface non-dimensional temperature, which is here fixed to 0.12 and is equivalent to a dimensional surface temperature of T_{surf} = 300 K, and $a(z)$ is the adiabatic correction at depth z. This correction is given by

$$a(z) = \exp\left[\int_0^z Di_S \frac{\alpha(z)}{C_P(z)} dz\right], \qquad (A15)$$

where Di_S is, again, the surface dissipation number, and $\alpha(z)$ and $C_P(z)$ the thermal expansion and heat capacity as a function of depth. These two functions are defined as part of the reference thermodynamical model involved in the compressible form of the conservation equations (Tackley, 1998). Practically, α decreases by a factor 5 from the surface to the CMB, while C_P is constant with depth. The adiabatic correction defined in Eq. (A15) then varies from 1.0 at the surface to about 1.55 at the CMB.

From temperature and composition to shear-wave velocity anomalies. To calculate shear-wave velocity (V_S) anomalies associated with thermo-chemical structures obtained by different simulations, we use the method developed in Deschamps et al. (2012), which involves the use of seismic sensitivities, *i.e.* partial derivatives of seismic velocities to temperature and various compositional parameters. For each model, temperature anomalies are calculated with respect to the radial profile of horizontally averaged temperature. Because the nature of regular ($C = 0$) and primordial ($C = 1$) material in thermo-chemical simulations are not *a priori* prescribed, they should be specified during the calculation of seismic velocity. Based on probabilistic tomography (Trampert et al., 2004; Mosca et al., 2012), we assumed that the regular composition is pyrolitic, and that the primordial material is enriched (compared to pyrolitic composition) in iron oxide by 3 %, and in bridgmanite by 18 %. Following this assumption, and accounting for the effect of post-perovskite, the relative V_S-anomalies (dlnV_S) are given by

$$\text{dln}V_S = \frac{\partial \ln V_S}{\partial T} dT + \frac{\partial \ln V_S}{\partial X_{Fe}} dX_{Fe} + \frac{\partial \ln V_S}{\partial X_{Bm}} dX_{Bm} + \frac{\partial \ln V_S}{\partial X_{pPv}} dX_{pPv}, \qquad (A16)$$

where dT, dX_{Fe}, dX_{Bm}, and dX_{pPv} are local anomalies in temperature, iron, bridgmanite, and post-perovskite. Practically, dT and dX_{pPv} are directly taken from the calculated distributions (after recalling for dT), and dX_{Fe} and dX_{Bm} are deduced from the compositional field following dX_{Fe} = Cd$X_{Fe,prim}$ and dX_{Bm} = Cd$X_{Bm,prim}$, where d$X_{Fe,prim}$ = 0.03, d$X_{Bm,prim}$ = 0.18. Sensitivities of V_S to temperature, iron, and bridgmanite are taken form Deschamps et al.

(2012) (Supplementary Figure S7), and were calculated from appropriate equation of state modelling and self-consistent mineralogical dataset. In the lowermost layer of tomographic model SB10L18 (Masters et al., 2000), in which the shear-wave velocity anomalies we calculated are averaged out, the average seismic sensitivities to temperature, iron, and bridgmanite are equal to -2.7×10^{-5} K^{-1}, -3.0×10^{-1}, and 0.33×10^{-1}, respectively. The sensitivity to post-perovskite is based on the compilation of Cobden et al. (2015), which include a more complete data set for this phase, and is and fixed to 2.0×10^{-2}.
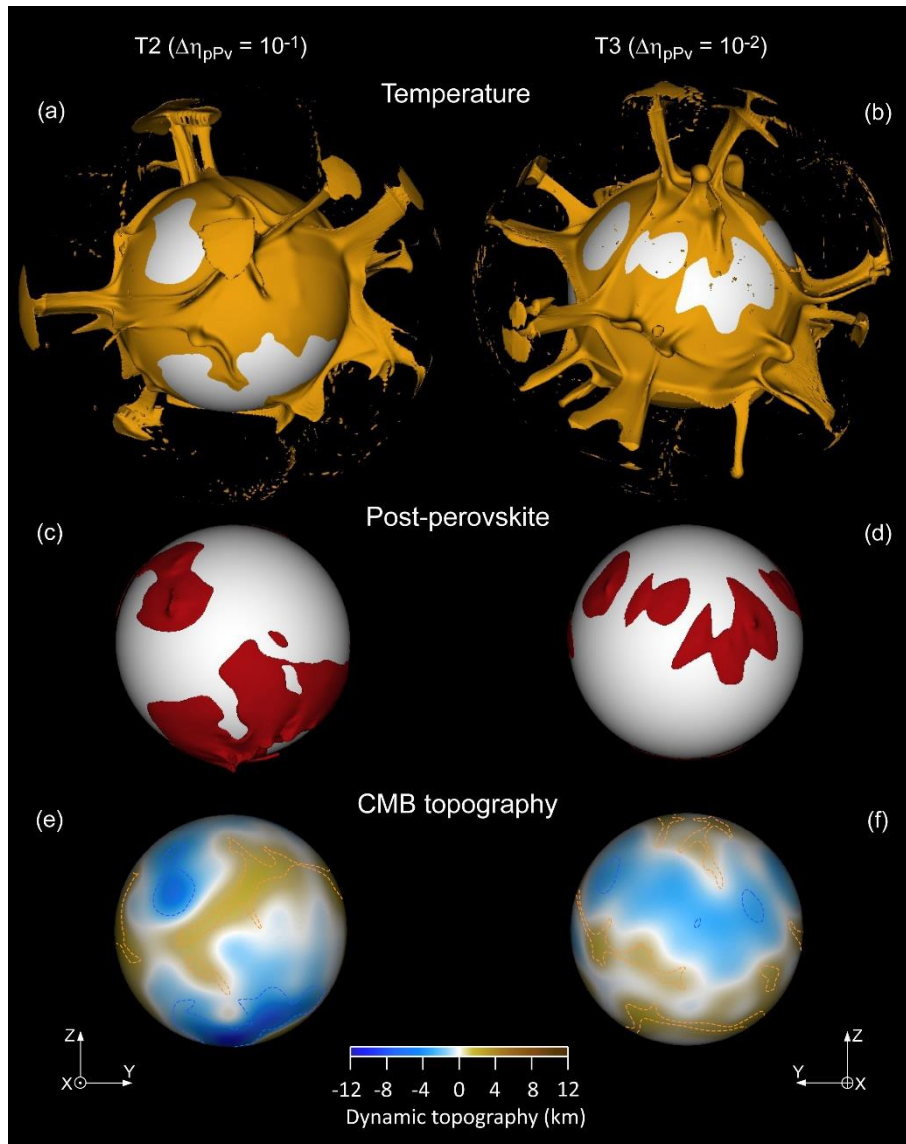

Figure S1. Snapshots of purely thermal cases with post-perovskite viscosity ratio $\Delta\eta_{pPv} = 10^{-1}$ (T2, left column) and $\Delta\eta_{pPv} = 10^{-2}$ (T3, right column) at non-dimensional time $t = 0.636 \times 10^{-2}$. (a) and (b) Isosurface of the non-dimensional temperature for $T = 0.80$. (c) and (d) Stability field of the post-perovskite phase. (e) and (f) Core-mantle boundary dynamic topography (color scale). The orange and blue dotted lines in plots (e) and (f) indicate the limits of the plumes and downwellings regions, respectively. Runs properties are listed in Table S1.
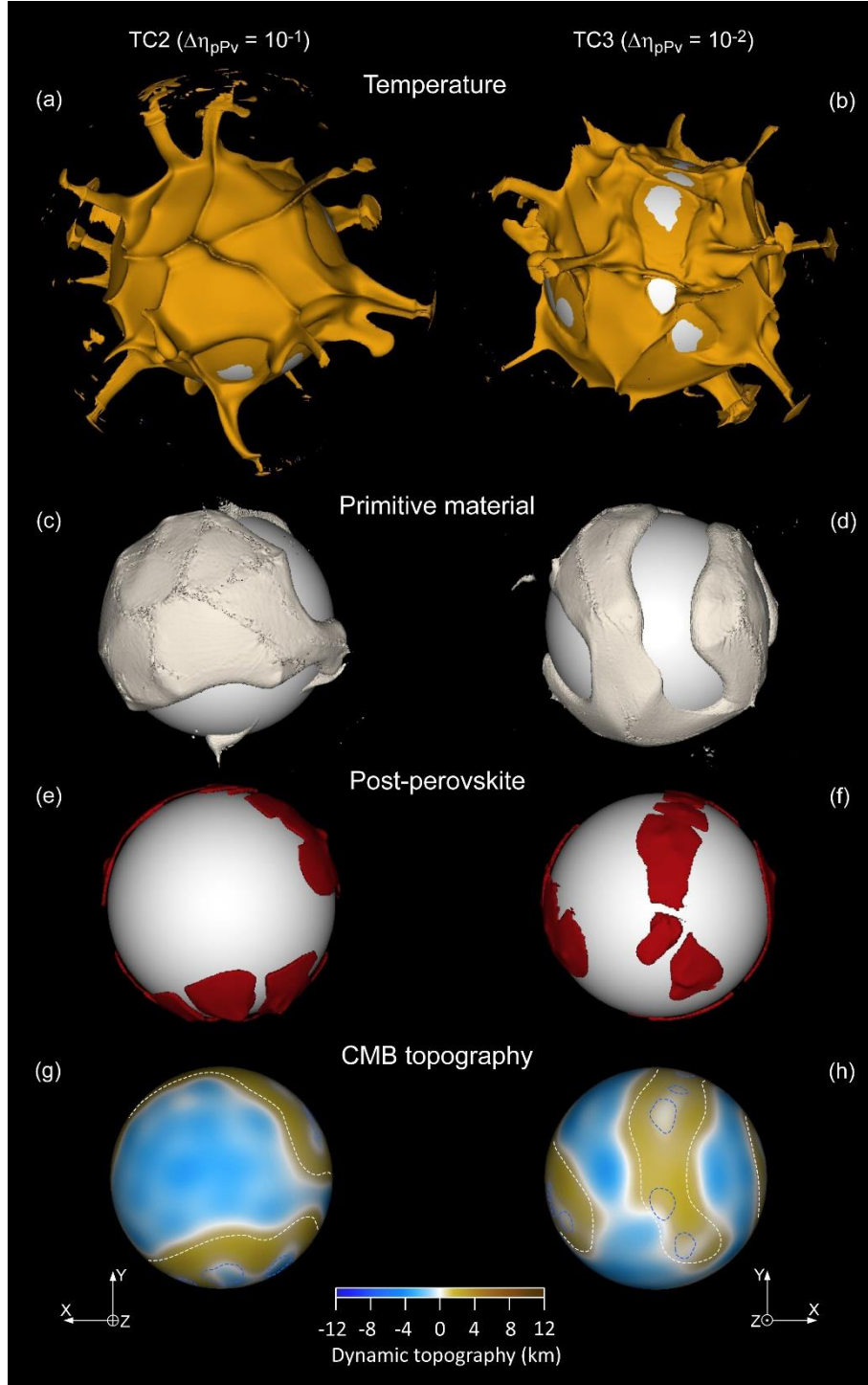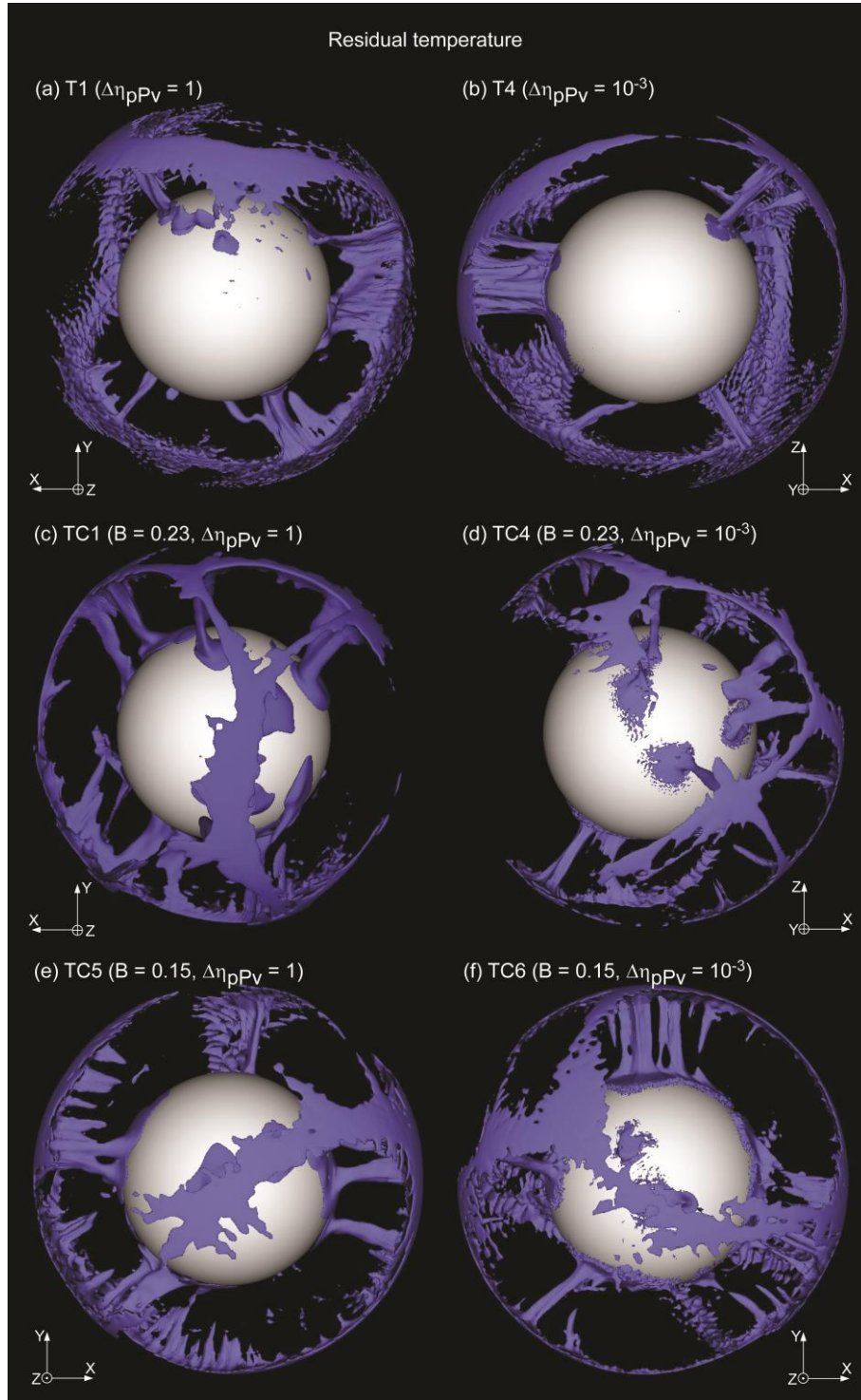
Figure S2. Snapshots of thermo-chemical cases with buoyancy ratio $B_z = 0.23$ and post-perovskite viscosity ratio $\Delta\eta_{pPv} = 10^{-1}$ (TC2, left column) and $\Delta\eta_{pPv} = 10^{-2}$ (TC3, right column) at non-dimensional time $t = 3.5 \times 10^{-2}$. (a) and (b) Isosurface of the non-dimensional temperature for $T = 0.70$ (TC2) and $T = 0.72$ (TC3). (c) and (d) Isosurface of the composition for $C = 0.5$. (e) and (f) Stability field of the post-perovskite phase. (g) and (h) Core-mantle boundary dynamic topography (color scale). The white and blue dotted lines in plots (g) and (h) indicate the limits of the reservoirs of dense material and of downwellings regions, respectively. Runs properties are listed in Table S1.
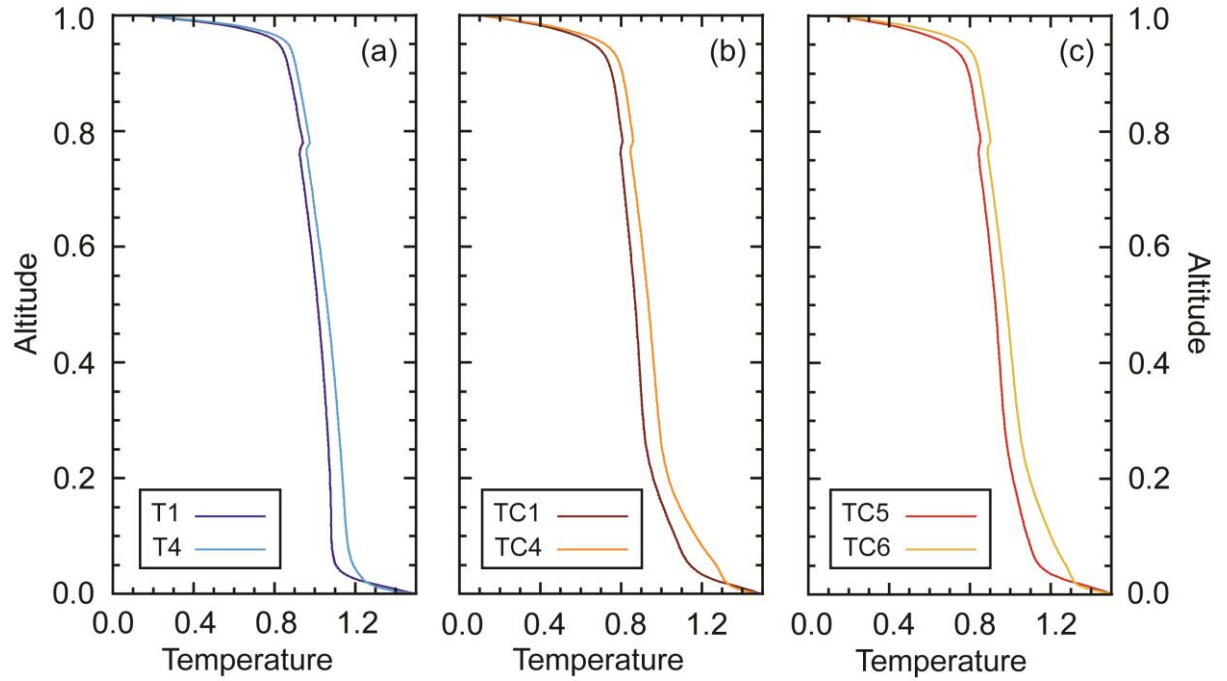
Figure S3. Radial profiles of the non-dimensional compressed temperature. (a) Purely thermal cases T1 ($\Delta\eta_{pPv} = 1$) and T4 ($\Delta\eta_{pPv} = 10^{-3}$) at non-dimensional time $t = 0.636\times10^{-2}$. (b) Strong thermo-chemical cases ($B_z = 0.23$) TC1 ($\Delta\eta_{pPv} = 1$) and TC4 ($\Delta\eta_{pPv} = 10^{-3}$) at non-dimensional time $t = 3.5\times10^{-2}$. (c) Weak thermo-chemical cases ($B_z = 0.15$) TC5 ($\Delta\eta_{pPv} = 1$) and TC8 ($\Delta\eta_{pPv} = 10^{-3}$) at non-dimensional times $t = 3.18\times10^{-2}$ and $t = 1.27\times10^{-2}$, respectively. Dimensional temperature can be obtained by rescaling non-dimensional temperature with super-adiabatic temperature jump $\Delta T_S = 2500$ K.

Figure S4. Snapshots of residual temperature showing downwellings. (a) and (b) Purely thermal cases T1 ($\Delta\eta_{pPv} = 1$) and T4 ($\Delta\eta_{pPv} = 10^{-3}$) at non-dimensional time $t = 0.636\times10^{-2}$. (c) and (d) Strong thermo-chemical cases ($B_z = 0.23$) TC1 ($\Delta\eta_{pPv} = 1$) and TC4 ($\Delta\eta_{pPv} = 10^{-3}$) at non-dimensional time $t = 3.5\times10^{-2}$. (e) and (f) Weak thermo-chemical cases ($B_z = 0.15$) TC5 ($\Delta\eta_{pPv} = 1$) and TC8 ($\Delta\eta_{pPv} = 10^{-3}$) at non-dimensional times $t = 3.18\times10^{-2}$ and $t = 1.27\times10^{-2}$, respectively.
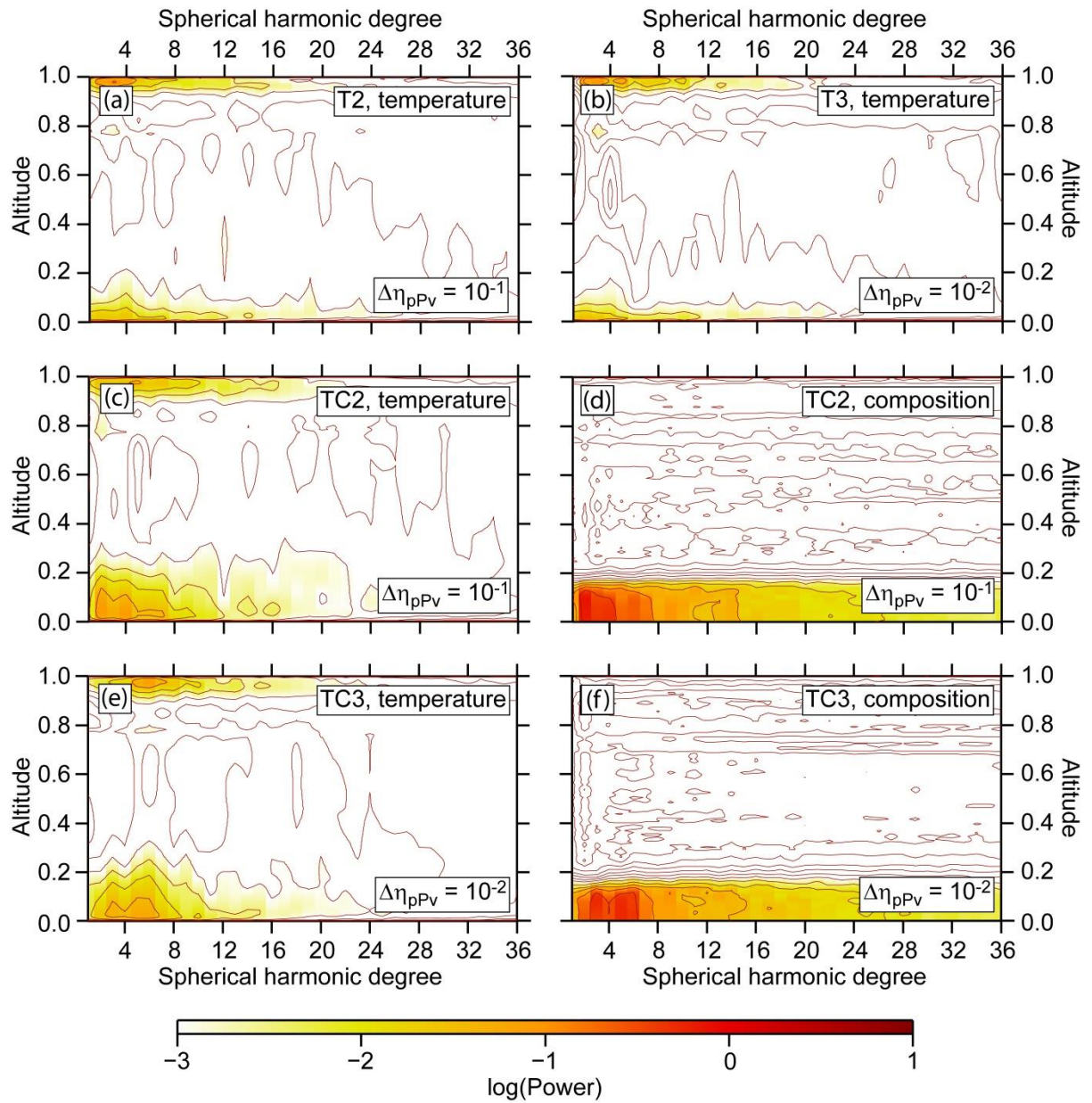
Figure S5. Spectral heterogeneity maps of temperature and compositional (if applicable) fields for purely thermal simulations T2 and T3, and thermo-chemical simulations TC2 and TC3. (a) Case T2. (b) Case T3. (c-d) Case TC2. (e-f) Case TC3. Power is plotted in logarithmic scale, and contour lines are plotted every log(*P*) = 0.5.
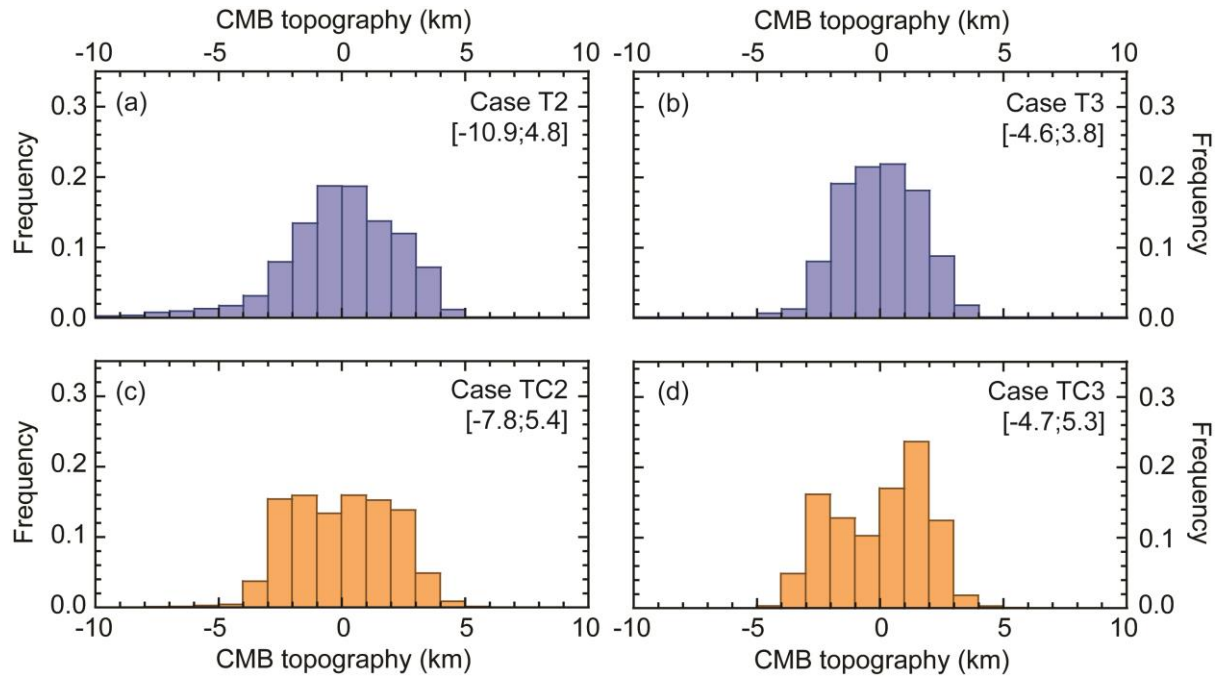
Figure S6. Distribution histograms of core-mantle boundary dynamic topography for purely thermal cases T2 and T3 (a and b), and thermo-chemical cases TC2 and TC3 (c and d). The brackets in legends indicate the topographic range (in km) for each case. The viscosity ratio between post-perovskite and bridgmanite is $\Delta\eta_{pPv} = 10^{-1}$ for cases T2 and TC2, and $\Delta\eta_{pPv} = 10^{-2}$ for cases T3 and TC3. In thermo-chemical cases, the buoyancy ratio is set to $B_z = 0.23$. All other properties are listed in Table S1. Frequency is normalized to the total area of the CMB. For convenience, histograms are truncated to the interval [-10; 10] km, implying that topography caused by downwellings in case T2 is not entirely represented.
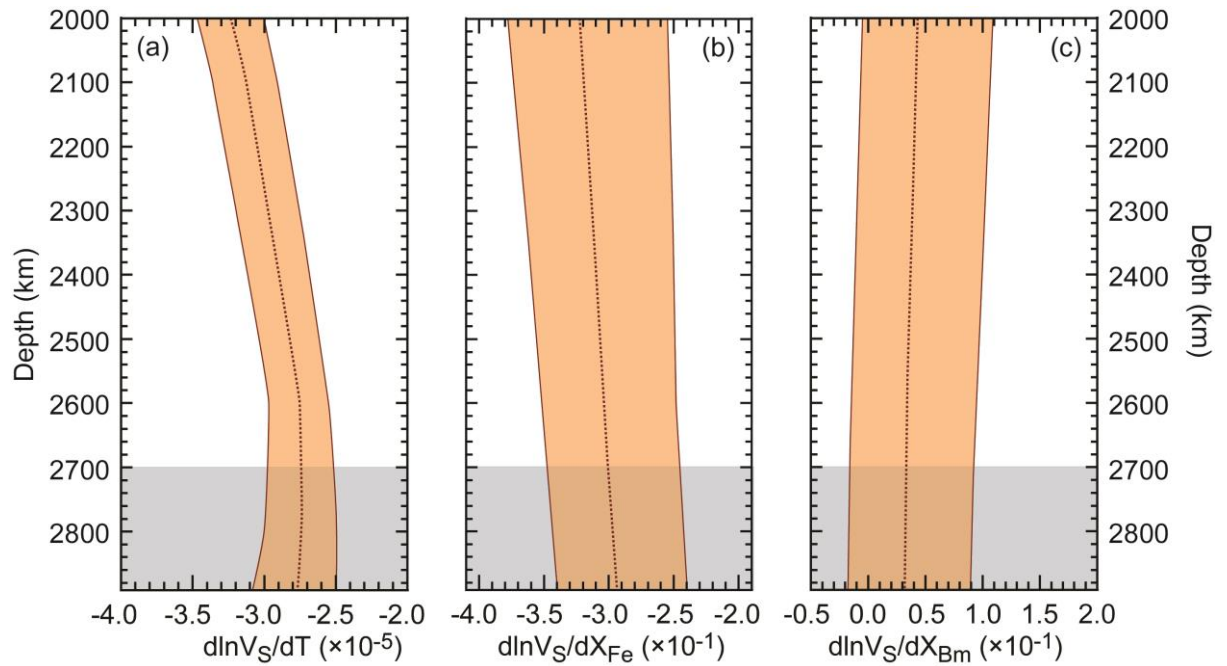
Figure S7. Sensitivities of shear-wave velocity to temperature (left), iron (middle), and bridgmanite (right). Sensitivities are taken from Deschamps et al. (2012) and are plotted in the depth range $2000 \leq z \leq 2891$ km. Dashed curves and colored areas show mean values in sensitivities and standard deviation, respectively. For calculation of seismic velocities in this study, we only used the mean values. The grey band at the bottom denote the vertical extension of the lower layer of tomographic model SB10L18, in which seismic velocities in Figures 8, 8, and S8 are averaged out.
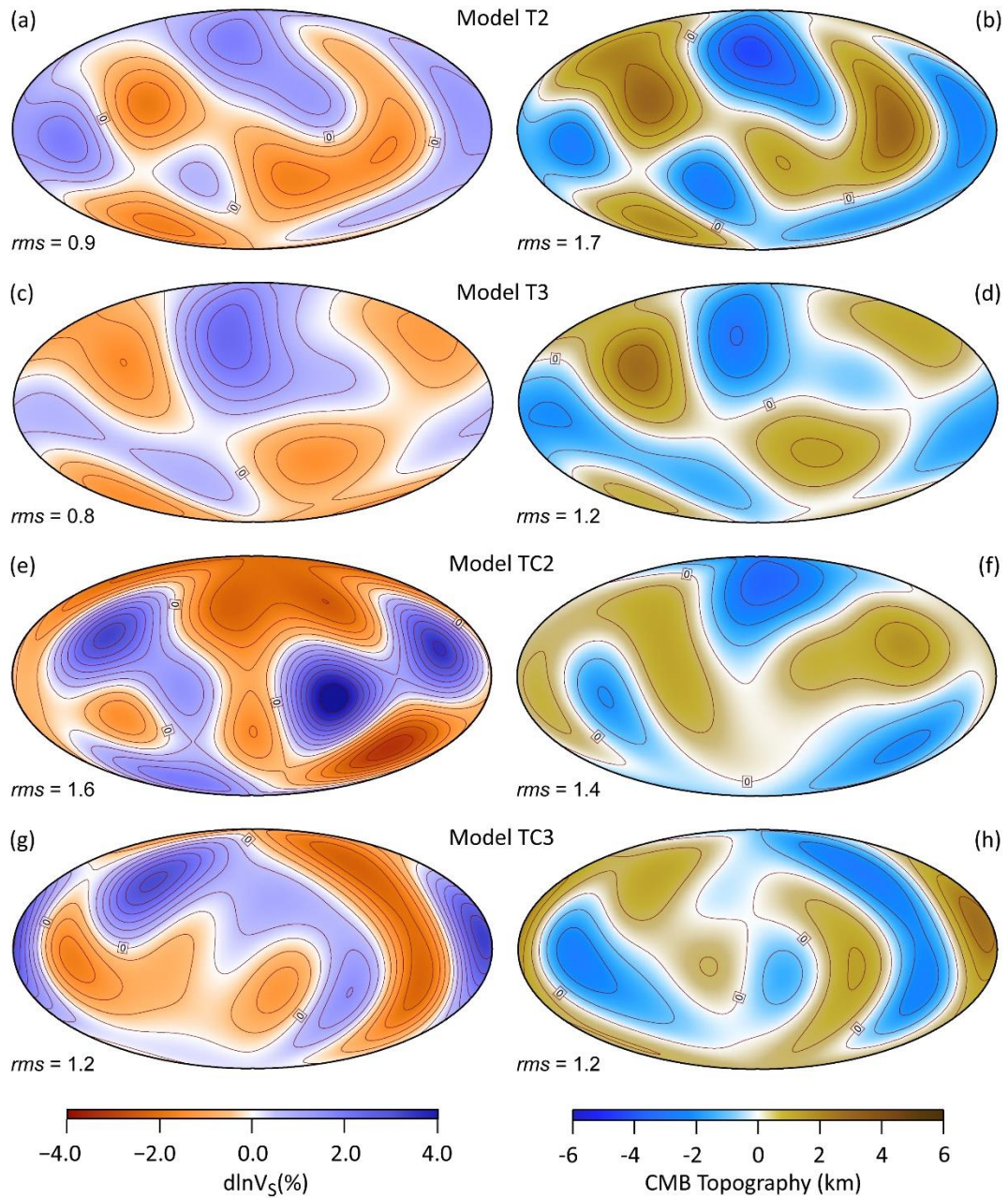
Figure S8. Shear-wave velocity anomalies in the lowermost mantle (2700-2891 km) (left column) and CMB dynamic topography (right column) predicted by purely thermal model T2 ($\Delta\eta_{pPv} = 10^{-1}$, first row) and T3 ($\Delta\eta_{pPv} = 10^{-2}$, second row), and thermo-chemical models TC2 ($\Delta\eta_{pPv} = 10^{-1}$, third row) and TC3 ($\Delta\eta_{pPv} = 10^{-2}$, last row). All maps are filtered for spherical harmonic degrees up to $l = 4$. For details on the calculation of shear-wave velocity anomalies, see main text and Supplementary Material. Interval of contour levels are 0.5% for dlnV_S and 1 km for CMB topography. Root mean square (*rms*) of each distribution is indicated at the bottom left of each plot.

Parameter	Symbol	Value	Units	Non-dimensional
Non-dimensional parameters				
Reference Rayleigh number	Ra_0			3.0×10^8
Surface dissipation number	Di_S			1.2
Volume average dissipative number	Di			0.43
Total internal heating	H_C	10	mW m^{-2}	4.8
Compositional heating ratio	ΔH_C	10		
Compositional parameters (for thermo-chemical models)				
Buoyancy ratio	B_z			0.15 - 0.23
Volume fraction of dense material (%)	X_{prim}			3.5
Physical & thermo-dynamical parameters				
Acceleration of gravity	g	9.81	m s^{-2}	1.0
Mantle thickness	D	2891	km	1.0
Reference adiabat	T_{as}	1600	K	0.64
Super-adiabatic temperature difference	ΔT_S	2500	K	1.0
Surface density	ρ_S	3300	kg m^{-3}	1.0
Surface thermal expansion	α_S	5.0×10^{-5}	K^{-1}	1.0
Surface thermal diffusivity	κ_S	6.24×10^{-7}	m^2 s^{-1}	1.0
Heat capacity	C_P	1200	J kg^{-1} K^{-1}	1.0
Surface conductivity	k_S	3.0	W m^{-1} K^{-1}	1.0
Surface Grüneisen parameter	γ_S	1.091		
Density jump at z = 660 km	$\Delta \rho_{660}$	400	kg m^{-3}	0.1212
Clapeyron slope at z = 660 km	Γ_{660}	-2.5	MPa K^{-1}	-0.0668
Post-perovskite density jump	$\Delta \rho_{pPv}$	62	kg m^{-3}	0.0188
Clapeyron slope of post-perovskite	Γ_{pPv}	13	MPa K^{-1}	0.3474
CMB temperature	T_{CMB}	3750	K	1.5
Density jump at CMB	$\Delta \rho_{CMB}$	5280	kg m^{-3}	1.6
Viscosity law				
Reference viscosity	η_0	1.6×10^{21}	Pa s	1.0
Viscosity ratio at z = 660 km	$\Delta \eta_{660}$	30		
Logarithmic thermal viscosity ratio	E_a	20.723		
Logarithmic vertical viscosity ratio	V_a	2.303		
Compositional viscosity ratio	$\Delta \eta_C$	30		
Post-perovskite viscosity ratio	$\Delta \eta_{pPv}$	10^{-3}-1		
Surface yield stress	σ_0	290	MPa	7.5×10^6
Yield stress gradient	$\dot{\sigma}_z$	0.01	Pa/Pa	0.01

Table S1. Parameters and scalings of numerical simulations of convection.